Effect of Bi Nanoprecipitates on the Thermoelectric Properties of Bi-Sb-Te/Sb₂O₃ Nanocomposites

Amir Pakdel,* Atta Ullah Khan, Florent Pawula, Sylvie Hébert, and Takao Mori*

BiSbTe-based nanocomposites hybridized with ceramic nanoparticles have recently revealed their higher efficiency as thermoelectric materials for near room-temperature applications, as compared to the traditional BiTe-SbTe alloys. Herein, the incorporation of ultra-small Bi nanoprecipitates into the microstructure of a $Bi_{0.5}Sb_{1.5}Te_3/Sb_2O_3$ nanocomposite and the consequential effects on the thermal and electrical transport properties of this three-phase hybrid system is reported. Electron microscopy characterization and systematic analysis of the thermoelectric properties of $Bi_{0.5}Sb_{1.5}Te_3/Sb_2O_3/Bi$ nanoprecipitate samples suggest that the minute Bi nanoprecipitates increase the charge carrier concentration of the nanocomposites, act as effective scattering sites throughout the microstructure, and shift the maximum Seebeck coefficient values to higher temperatures.

1. Introduction

The shortage of fossil fuel resources and the global climate change associated with fuel-burning to produce electricity have raised awareness about the importance of renewable energy sources.[1,2] Among the various sustainable power production technologies, thermoelectric generation is an environmentally friendly alternative where a temperature difference between a thermoelectric generator (TEG) and its surrounding ambient can be converted to electricity in a solid-state manner.[3,4] Thus, this technology makes it possible to harvest the thermal energy from a heat source (such as motor vehicles, furnaces, or the human body) pollution-free, motion-free, and noise-free, and convert it to electrical energy.[5–9] In this regard, there has been an increasing need to develop thermoelectric materials with high efficiency near room temperature, for usage in TEGs to charge batteries in low-power electronic devices such as the Internet of Things sensors.[10–13]

Bismuth telluride (Bi_2Te_3) based alloys have been a classical thermoelectric material for near room-temperature applications, both due to their high conversion efficiency and commercial upscaling maturity.[14,15] BiSbTe alloys in particular are the most studied inorganic p-type thermoelectric materials; therefore, much effort has been devoted to enhancing their thermoelectric properties, such as reduction of the lattice thermal conductivity,[16] optimization of charge carrier concentration,[17] and hybridization with a second phase (usually a nanomaterial):, for example, Sb_2O_3,[18] $AgSbSe_2$,[19] Si,[20] Te,[21] $LaFeSi$,[22] $AgSbTe_2$,[23] $BaTiO_3$,[24] MgO/VO_2,[25] $AgBiSe_2$,[26] Sb_2Te_3,[27] SiO_2,[28] Y_2O_3,[29] Zn_4Sb_3,[30] SiC,[31] TiC,[32] ZnO,[33] ZnAlO,[34] Pr_6O_{11},[35] $CuGaTe_2$,[36] Cu_3SbSe_4,[37] ZnTe,[38] ZrO_2,[39] Ta_2O_5,[40] amorphous B,[41] graphene,[42] and C fibres.[43,44] Moreover, various nanoengineering approaches, such as severe plastic deformation and melt spinning, have been used to improve the thermoelectric performance of BiSbTe alloys.[45,46]

There are very few reports on the thermoelectric behavior of BiSbTe-based composites hybridized with two different components, for example, co-dispersed Cu and HfO_2 nanoparticles,[47] and TiO_2–Ag nanoparticles,[48] perhaps due to the complexity of transport behavior analysis in such ternary systems. Having previously demonstrated outstanding thermoelectric performance of $BiSbTe/Sb_2O_3$ nanocomposites and their excellent thermal and chemical stability in the ambient atmosphere up to 475 K,[18] in this work we have added Bi nanoprecipitates (that may also be regarded as nanodots due to their ultra-small size) as the third phase to $BiSbTe/Sb_2O_3$ and investigated the electronic and thermal transport behavior of this ternary nanocomposite system. Nanodots can be very effective in phonon scattering;[49–50] however, there have been very few reports on their incorporation into inorganic thermoelectric systems, for example, Cu_2Se/C nanodots,[51] CdSe/Pd nanodots,[52] SnSe/Au nanodots,[53] and SnSe/Se nanodots,[54] mostly due to complex synthesis routes of such hybrid materials. Herein, we present a facile method to synthesize BiSbTe/Bi nanodots, followed by hybridization with Sb_2O_3 nanoparticles, which led to a striking thermoelectric performance near room temperature and even at higher temperatures up to 475 K.

A. Pakdel
Department of Mechanical
Manufacturing & Biomedical Engineering
Trinity College Dublin
The University of Dublin
Dublin D02PN40, Ireland
E-mail: pakdela@tcd.ie

A. U. Khan, T. Mori
International Center for Materials Nanoarchitechtonics (WPI-MANA)
National Institute for Materials Science (NIMS)
Namiki 1-1, Tsukuba 305-0044, Japan
E-mail: MORI.Takao@nims.go.jp

F. Pawula, S. Hébert
Normandie University
ENSICAEN, UNICAEN, CNRS, CRISMAT, UMR6508
14000 Caen, France

⬡ The ORCID identification number(s) for the author(s) of this article can be found under https://doi.org/10.1002/admi.202200785.

**ADVANCED
SCIENCE NEWS**
www.advancedsciencenews.com

**ADVANCED
MATERIALS
INTERFACES**
www.advmatinterfaces.de

2. Results and Discussion

2.1. Microstructure and Chemical Composition

Samples with a nominal composition of $Bi_{0.5}Sb_{1.5}Te_3$ (from now on referred to as BST) with additional Bi content equal to 1, 1.5, and 2 wt.% are labeled Bi-1, Bi-1.5, and Bi-2, respectively. **Figure 1**a shows a typical scanning electron microscopy (SEM) image of a sintered and ground BST/Sb_2O_3/Bi-2 nanocomposite comprising micro-and nano-sized powders of BST (with additional 2 wt.% Bi) and Sb_2O_3 nanoparticles. The corresponding energy-dispersive spectrometry (EDS) spectrum in Figure 1b indicates the peaks of Bi, Sb, Te, and O from the ground mixture, while the other peaks (Al, C, and Be) are associated with the SEM sample holder, detector, and substrate. The X-ray diffraction (XRD) pattern in Figure 1c was obtained from the same compositional sample after SPS. All the present peaks could be indexed to the $Bi_{0.5}Sb_{1.5}Te_3$ phase (JCPDS card 49–1713), with an R-3m rhombohedral structure. In the magnified XRD pattern in Figure 1d, a small peak of the Sb_2O_3 phase (121), with an orthorhombic structure (Pccn space group No. 19, P-$2_12_12_1$), could be identified in the shoulder of the BST (105) peak. However, considering the small amount of additional Bi content, no obvious tertiary phase could be identified from the XRD pattern. One must note that even the most modern XRD machines have a detection limit of ≈1 vol.%, therefore, when a chemical element or compound is present below this level, the noise will be stronger than the corresponding peaks. In such cases, more sensitive methods such as electron microscopy will be required for accurate characterization of the sample, as shown below.

Low/high magnification SEM images in Figure 1e–h show the fracture surface of a BST/Sb_2O_3/Bi nanocomposite sample consolidated by SPS. Figure 1e indicates grain orientation anisotropy in the sample. In low magnification Figure 1e,f a distribution of Sb_2O_3 nanoparticles in the BST matrix is visible. However, high magnification Figure 1g,h displays the presence of a nanometre-sized third phase in the sample. To further characterize this third phase, transmission electron microscope (TEM) and STEM methods were utilized. A representative bright-field STEM image of the nanocomposite is shown in **Figure 2**a, demonstrating the presence of oxide nanoparticles in the grain boundaries of the BST matrix, and a broad-range distribution of very small nanoprecipitates. Figure 2b shows all these three phases in higher magnification. It looks as if some of the matrix grains are covered by high concentrations of these ultra-fine nanoprecipitates in close vicinity of each other, which might be regarded as a network. Figure 2c is a high-angle annular dark-field (HAADF) STEM image of the same location on the sample as in Figure 2a. HAADF images are very sensitive to atomic number variations in the sample (Z-contrast images). Elements with a higher atomic number appear brighter in the image and vice versa. Figure 2c clearly illustrates three phases: the BST matrix, Sb_2O_3 nanoparticles in a darker color (due to lower atomic number of oxygen), and a very fine network of nanoprecipitates in white color (suggesting the presence of the heaviest element, i.e., bismuth). The higher magnification image in Figure 2d suggests that the individual nanoprecipitates could be of the size of ≤ 1 nm. Because of the ultimately small sizes, it is difficult to contrast the nanoprecipitates in high-resolution TEM images in Figure 2e,f, but the high crystallinity of the BST matrix is distinctive.

In situ chemical analysis of the sample was performed using EDS in the dark field STEM mode. Figure 2g shows the distinct nanoprecipitate networks (point 1: white color) and oxide nanoparticles (point 2: black color) in the BST matrix (grey color). The corresponding EDS point analyses in point 2 confirm that the white nanoprecipitates are composed of Bi (either pure Bi or a highly Bi-rich composition, but not bismuth oxide), in contrast with point 1 results that clearly show strong peaks of Sb and O. The other EDS peaks in each case come from the surrounding and underneath area on the sample; nevertheless, the comparison between the EDS spectra provides conclusive evidence on the chemical composition of each phase. Larger size and more detailed EDS spectra are available in Figure S1, Supporting Information.

2.2. Thermoelectric Properties

Figure 3a shows the temperature dependence of electrical conductivity in BST/Sb_2O_3 and BST/Sb_2O_3/Bi nanocomposites. The electrical conductivity decreases with temperature in all samples, as is common in heavily doped semiconductors which have transport property temperature dependences similar to metals, that is, $d\sigma/dT < 0$. It is also noticeable that the addition and increasing of Bi nanoprecipitate content considerably improved the electrical conductivity in the whole tested temperature range. The room-temperatures electrical conductivity of BST/Sb_2O_3 was enhanced by 24.3%, 49.4%, and 68.5% by adding 1, 1.5, and 2 wt.% Bi nanoprecipitates, respectively. The complete set of measured data is provided in Figure S2, Supporting Information. The maximum deviation from the reported values of electrical conductivity at all measured temperatures in Figure 3a was 15.4% for BST/Sb_2O_3/Bi-1, 16.7% for BST/Sb_2O_3/Bi-1.5, and 12.1% for BST/Sb_2O_3/Bi-2.

The electrical conductivity of elemental Bi at room temperature is considerably larger than that of BST/Sb_2O_3 (around an order of magnitude) as Bi is a semimetal.[55,56] In the case of nano-size Bi structures, however, it is believed that the semimetallic behaviour of Bi might change to semiconducting (n-type). An example of electronic behavior size-dependency in Bi nanostructures describes that a decrease of Bi nanotube wall thickness from 100 to 15 nm resulted in a metal–semiconductor transition.[57] Another study shows that the bandgap in Bi nanowires opened up by reducing the diameter from 15 to 9 nm.[58] On the other hand, Stokes and co-workers have reported that the incorporation of 5% and 7% Bi nanoparticles of 10–20 nm size into a Bi_2Te_3 matrix almost doubles the electrical conductivity values due to the metallic nature of Bi nanoinclusions and the consequent carrier concentration increase in Bi_2Te_3/Bi composites.[59]

To understand whether the Bi nanoprecipitates behave as semimetals or semiconductors in a BST/Sb_2O_3/Bi nanocomposite system, further complex theoretical calculations are required. But either way, the direct relationship between electrical conductivity enhancement and additional Bi nanoprecipitates in our BST/Sb_2O_3 nanocomposites requires a mechanism to conduct the
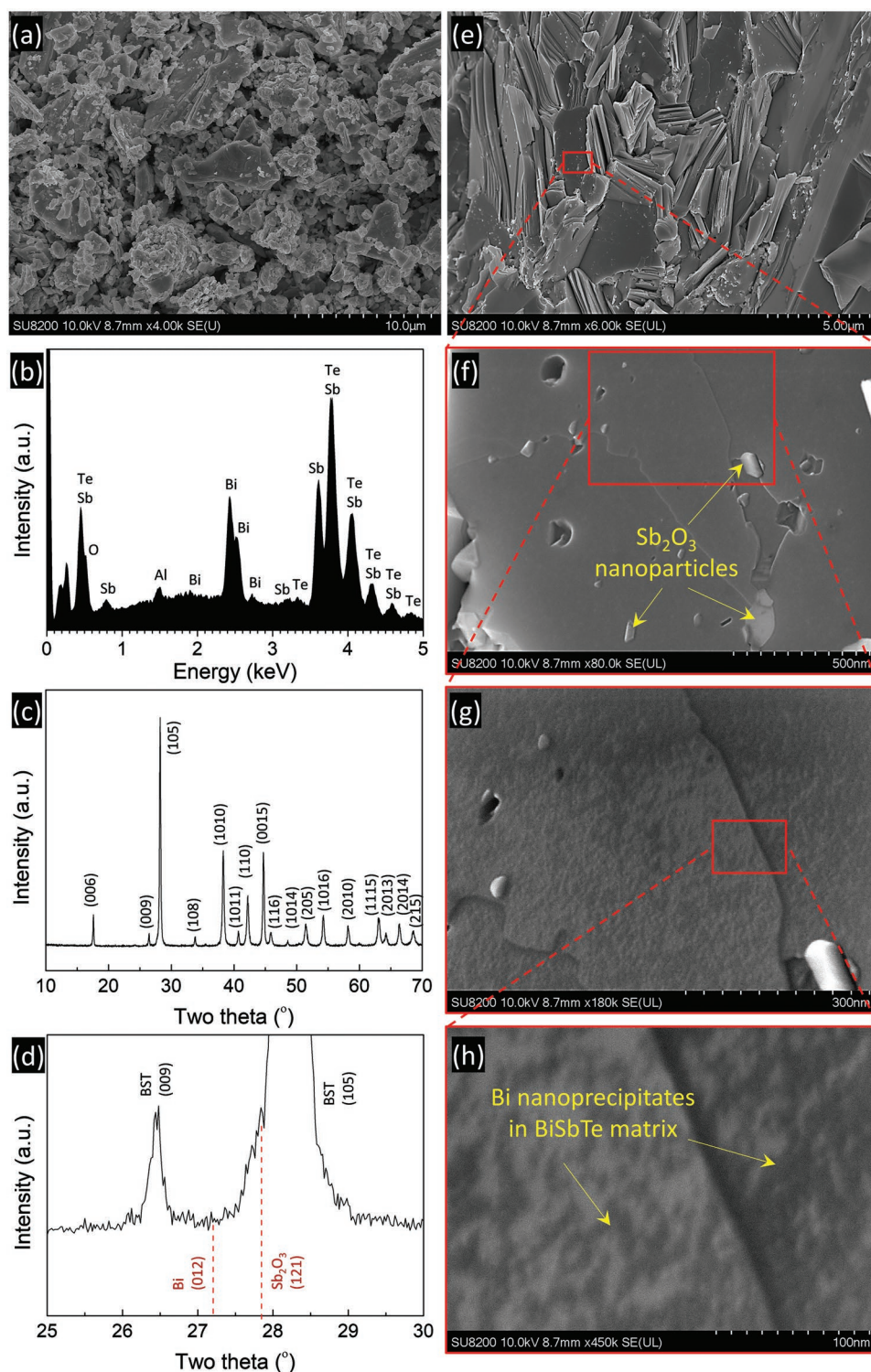
Figure 1. a,b) SEM image and EDS analysis of mixed BST/Sb$_2$O$_3$/Bi. c,d) XRD patterns of a nanocomposite sample. e–h) HR-SEM images illustrate an ultimately small nanoprecipitate phase distributed in the BST/Sb$_2$O$_3$ nanocomposite.

additional charge carriers between the Bi nanoprecipitates. This could be via tunneling between nanoprecipitates,[60] since they are located close together, arranging a network as evidenced by the TEM micrographs in Figure 2. There are theoretical studies

suggesting that the electrical conductivity in quantum-sized arrays may be understood in a t–U Hubbard model where the hopping integral t and the on-site Coulomb correlation U can be controlled by quantum dot coupling and composition.[50]

2200785 (3 of 11)

**ADVANCED
SCIENCE NEWS**

www.advancedsciencenews.com

**ADVANCED
MATERIALS
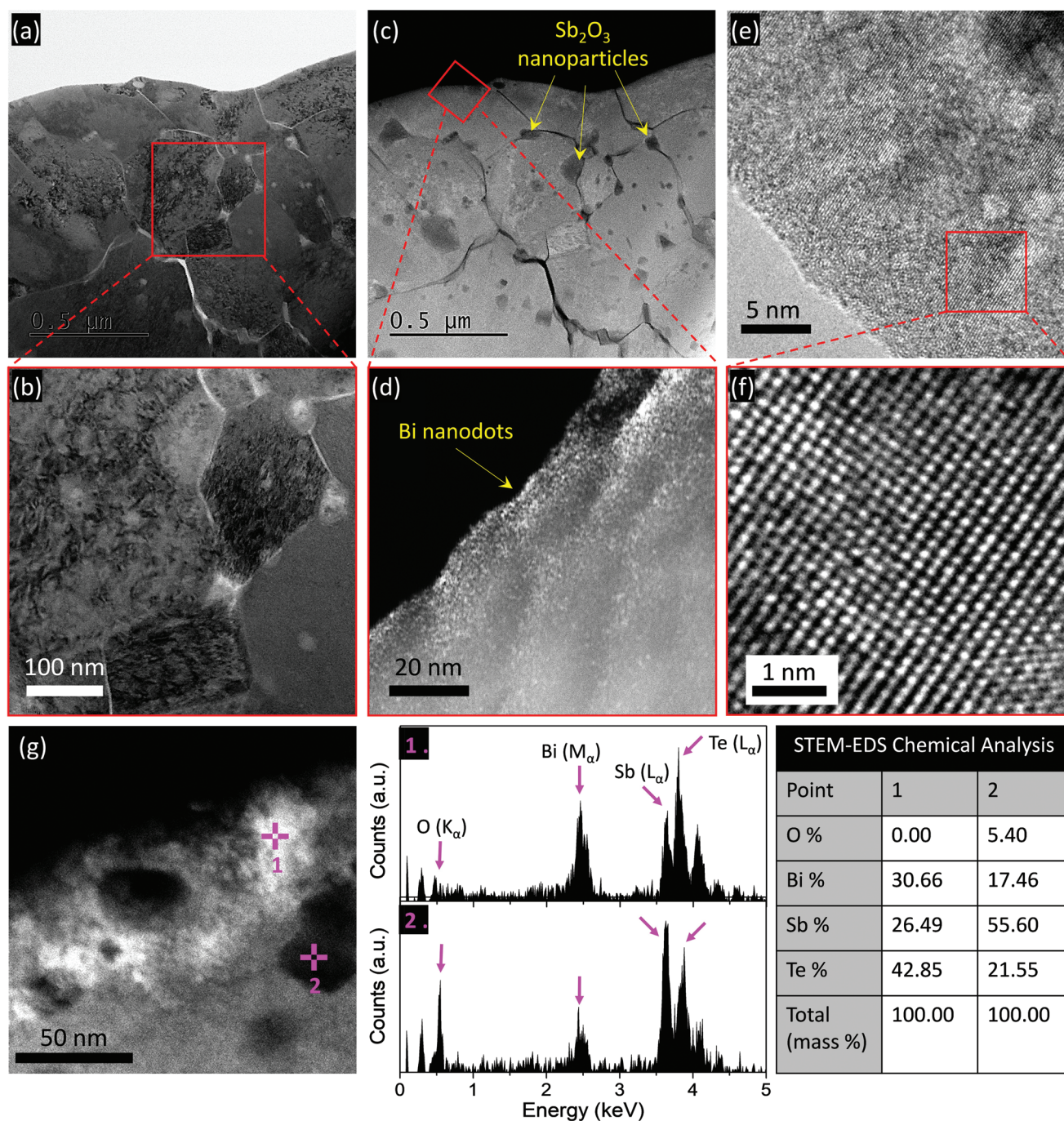INTERFACES**

www.advmatinterfaces.de

Figure 2. a,b) Bright-field STEM analysis demonstrating the presence of three different phases. c,d) Dark field STEM analysis showing the ultimately small nanoprecipitates with sizes ≤ 1 nm in the composite. e,f) High-resolution TEM, confirming the good crystallinity of the sample. g) Dark-field STEM and EDS analysis of the Bi nanoprecipitates and oxide nanoparticles.

The electrical conductivity of a p-type semiconductor is a function of its carrier (hole) concentration p and mobility μ, described as $\sigma = \mu.p.e$, where e is the carriers charge. However, if minority charge carriers (electrons) have a non-negligible contribution to electrical conduction, the total electrical conductivity may be expressed as a linear combination of hole and electron conductivities (σ_h and σ_e, respectively) in a simple two-band system. More complex systems would consider

an additional impurity band for a multi-band conduction approach.[61] The Hall effect measurements in Figure 3b show that the variation of an effective charge carrier concentration ($\bar{p}$) with temperature was negligible in all samples between 300 and 375 K. The term "effective" charge carrier concentration is used here, since it was calculated from the Hall coefficient data obtained by the Van der Pauw method (Figure S3, Supporting Information). This Hall coefficient measuring configuration
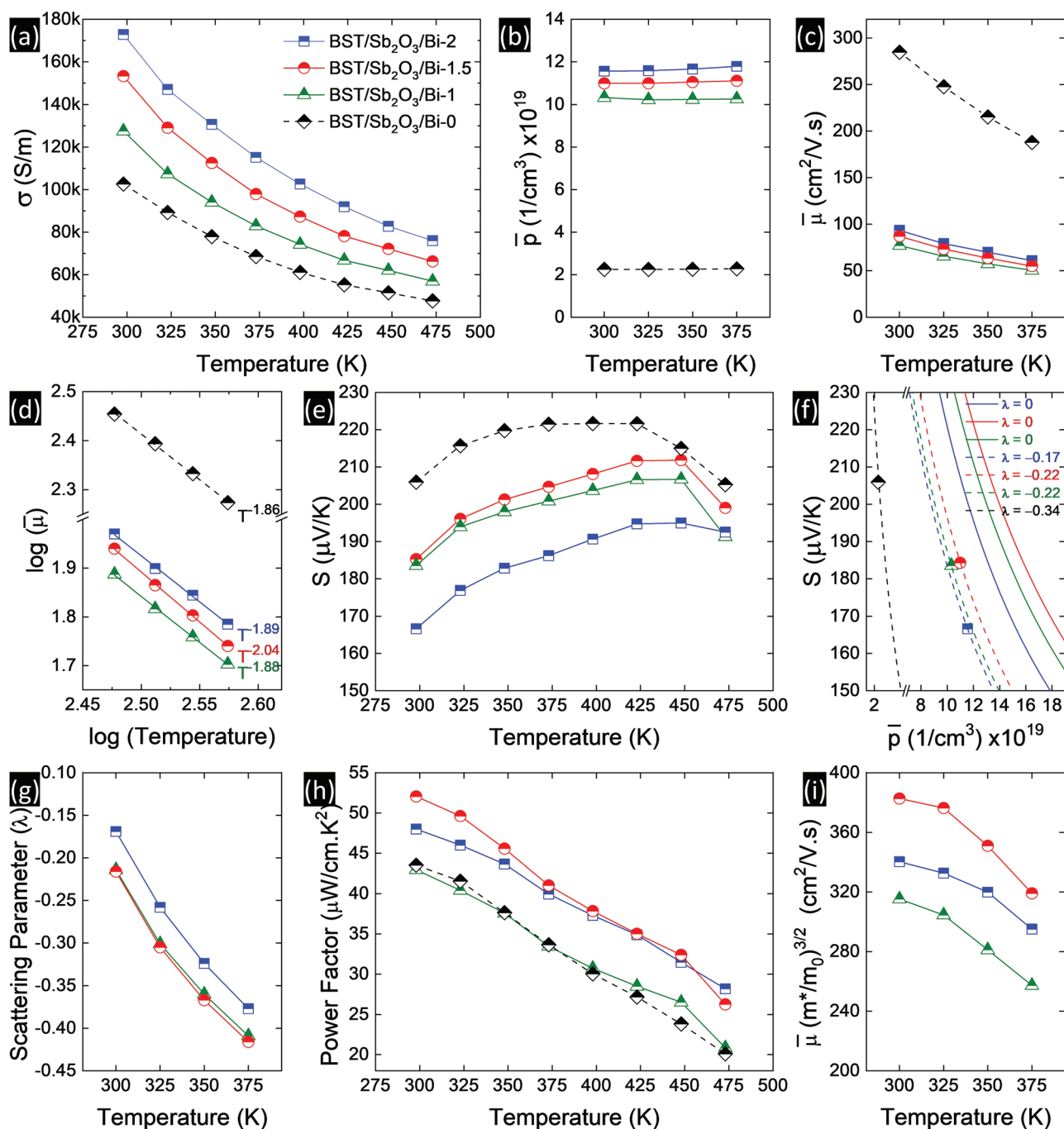
2200785 (4 of 11)

Figure 3. Temperature dependence of a) electrical conductivity, b) charge carrier concentration, and c) charge carrier mobility in BST/Sb_2O_3/Bi nano-composites. d) Measurement of parameter x in the temperature dependence of mobility described as $\mu \propto (KT)^x$. e) Temperature dependence of the Seebeck coefficient. f) Seebeck coefficient versus charge carrier concentration (Pisarenko lines) at 300 K. Temperature dependence of g) SPB scattering parameter, h) power factor, and i) weighted mobility in BST/Sb_2O_3/Bi nanocomposites.

does not render information about the potential presence of different types of charge carriers. The slight increase of $\overline{p}$ with temperatures can be attributed to the thermal activation of electron-hole pairs occurring at higher temperatures.[16] Similarly, the decline of effective mobility $\overline{\mu}$ with temperature in Figure 3c is due to increasing electron-phonon interactions at higher temperatures. **Figure 4**b,c also demonstrate that

BST/Sb_2O_3/Bi-nanoprecipitate samples had higher effective carrier concentration and lower effective carrier mobility as compared to the reference BST/Sb_2O_3 sample, which suggests larger scattering effects in nanoprecipitate composite samples. This is in agreement with other reports on carrier scattering at heterojunction potentials in BST composites with nano-inclusions.[37,62] Therefore, we can conclude that the electrical
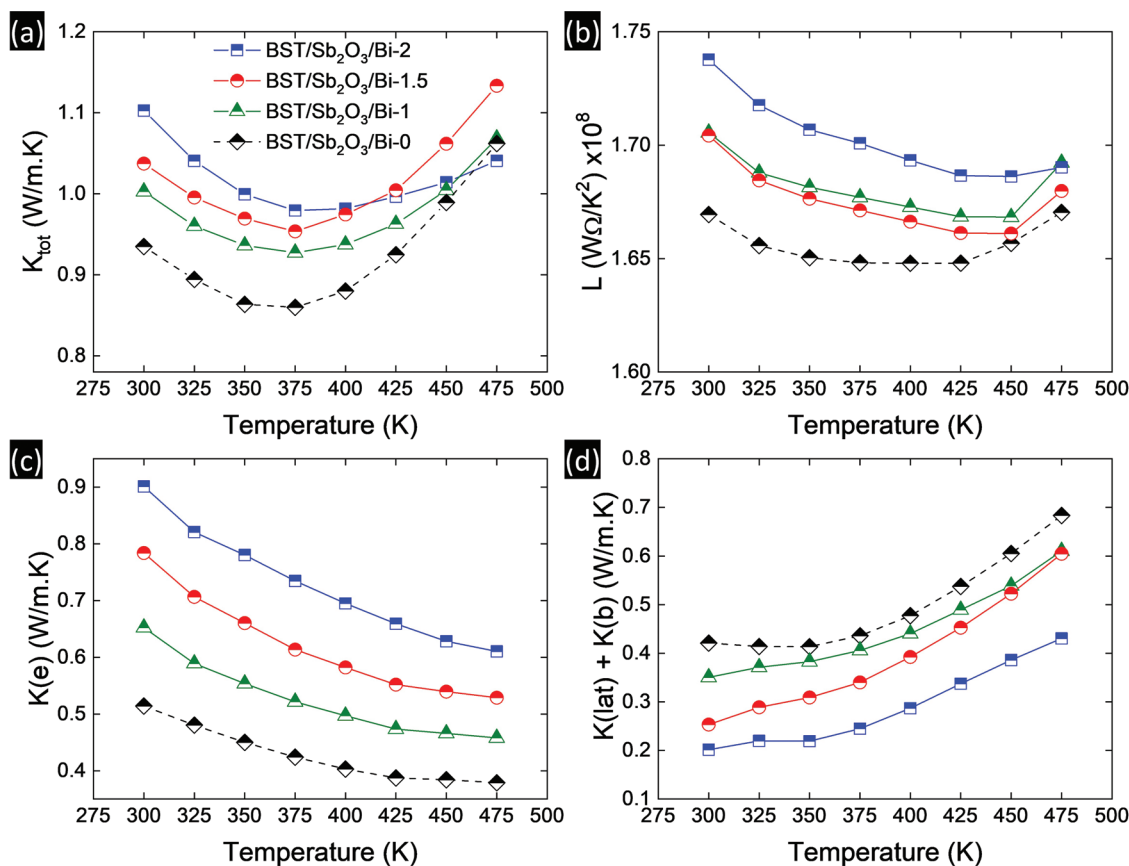
**ADVANCED
SCIENCE NEWS**

www.advancedsciencenews.com

**ADVANCED
MATERIALS
INTERFACES**

www.advmatinterfaces.de

Figure 4. Temperature dependence of a) total thermal conductivity, b) Lorenz number, c) electrical component of thermal conductivity, and d) lattice and bipolar components of thermal conductivity in $BST/Sb_2O_3/Bi$ nanocomposites.

conductivity of BST/Sb_2O_3 was enhanced by adding Bi nanoprecipitates, mainly due to enhanced carrier concentrations.

Figure 4b,c also shows that both effective charge carrier concentration and the corresponding effective mobility had a direct relationship with Bi nanoprecipitate content. That is:

$$\overline{p}, \overline{\mu} : \text{Bi-1} < \text{Bi-1.5} < \text{Bi-2} \tag{1}$$

Bismuth telluride-based alloys are well known to have non-stoichiometric compositions with Te-deficiency; therefore, a partial substitution of Bi from Bi nanoprecipitates into the BST lattice (antisite defects) during synthesis and sintering is a valid assumption for our samples. This could explain the increase of $\overline{p}$ with Bi nanoprecipitate content, as Bi-antisite defects each contribute one hole per defect. Higher levels of Bi substitution lead to further formation of charged BST/Bi-nanoprecipitate interfaces that can inject excess charge carriers into the core of BST grains and increase the charge carrier concentration in Bi-2 sample as compared to Bi-1 sample for instance. It should be reminded that p values in Figure 3b represent effective carrier concentrations that could also contain an electron-related component in addition to the hole-related component. That is, if n-type Bi nanoprecipitates form new energy states (or bands) near the Fermi level of the BST matrix and contribute electrons to the conduction band, that could also affect the $\overline{p}$ value. In the case of mobility, however, the higher Bi content

could lead to agglomeration of the nanoprecipitates and the formation of a somewhat continuous network (as shown in high-magnification SEM and TEM images), which means an easier flow path for the charge carriers passing through Bi nanoprecipitates rather than facing numerous BST/Bi interfaces. This has previously been reported for graphene quantum dots embedded in Bi_2Te_3.[63] Nevertheless, the values of $\overline{p}$ and $\overline{\mu}$ in all $BST/Sb_2O_3/Bi$ nanocomposites are very close together, but immensely different from those of the reference BST/Sb_2O_3 sample, suggesting the large influence of Bi nanoprecipitates on charge transport properties.

The charge carrier mobility in a semiconductor gives information about the nature of transport, and when plotted against temperature, the dominant carrier scattering mechanism can be deduced.[64] Considering conduction in a single parabolic band (SPB), the temperature dependence of mobility can be described by power-law when a single scattering mechanism limits μ:

$$\mu \propto T^x \tag{2}$$

where the exponent x is a representative of the scattering process. An exponent x equal to $-3/2$, 0, or $3/2$ indicates scattering by acoustic phonons, neutral impurities, or ionized impurities, respectively. Polar and non-polar optical phonon scattering processes can contribute to a slope of $-1/2$ to $-5/2$. Phonon scattering (both polar and non-polar) and ionized impurity

scattering are the predominating mechanisms at low electric fields, and other mechanisms such as carrier-carrier scattering and intervalley scattering may be generally omitted to a first approximation.[65]

Figure 3d shows a plot of log[μ] versus log[T] for all samples between 300 and 375 K, where the slope of each line represents the exponent x. In BST/Sb$_2$O$_3$ the slope is −1.86 and by adding Bi nanoprecipitates the slope becomes more negative, that is, between −1.89 and −2.04. These values suggest phonon scattering to be the main scattering mechanism, and perhaps a combination of acoustic and optical phonon scattering. It can be assumed that at room temperature, optical and acoustic phonons contribute to scattering with comparable weight, but at higher temperatures, optical phonons will be more effective than acoustic phonons.[65] That could be a reason for the slope of the graph in Figure 3d to be larger than the theoretically predicted −3/2 (further discussion available in Figure S4, Supporting Information). Furthermore, research on other thermoelectric materials has also demonstrated major deviations from the theoretical prediction, especially when the material properties were temperature-dependent. For example, the decay of mobility in Pb-Te with a rate of $T^{-2.5}$ has been attributed to its temperature-dependent effective mass of electrons (m*). Similarly, temperature-dependent mobility rates of $T^{-1.9}$ in n-type Ba-Ga-Ge, $T^{-1.94}$ in p-type Bi-Te, and $T^{-1.63}$ in n-type Bi-Te alloys have been previously reported.[66–67] In general, when Hall mobility declines rapidly with temperature, it indicates that acoustic phonon scattering limits μ.[64] Therefore, adopting the SPB model for transport behavior in our BST nanocomposites at near-room temperature ranges could be relevant.

Figure 3e displays the Seebeck coefficient (S) of p-type BST/Sb$_2$O$_3$/Bi nanocomposites between 300 and 475 K. The Seebeck coefficient of all samples increased with temperature initially and upon reaching a maximum value decreased. This is due to the well-known bipolar thermodiffusion effect occurring at higher temperatures because of the excitation of minority carriers (i.e., electrons) and the thermal activation of electron-hole pairs (further discussion available in Figure S5, Supporting Information). The Seebeck coefficient in all BST/Sb$_2$O$_3$/Bi nanocomposites had smaller values than in the reference BST/Sb$_2$O$_3$ sample, consistent with the conductivity increase with Bi addition. Moreover, hot-pressed samples of semiconducting Bi nanoparticles have demonstrated negative Seebeck coefficients between −55 and −146 μV K^{-1}, depending on the particle size and sintering conditions.[68,69] That can explain why the Seebeck coefficients of all BST/Sb$_2$O$_3$/Bi samples were smaller than that of the reference BST/Sb$_2$O$_3$. The complete set of measured data is provided in Figure S2, Supporting Information. The maximum deviation from the reported values of the Seebeck coefficient at all measured temperatures in Figure 3e was 9.2% for BST/Sb$_2$O$_3$/Bi-1, 3.1% for BST/Sb$_2$O$_3$/Bi-1.5, and 7.1% for BST/Sb$_2$O$_3$/Bi-2.

Among BST/Sb$_2$O$_3$/Bi nanocomposites, the Bi-1.5 and Bi-1 samples had close S values (1-3% difference) but the Bi-2 sample had lower S values as compared to them (8%–12% lower). The maximum S in Bi-1, Bi-1.5, and Bi-2 samples were 207, 212, and 195 μV k^{-1}, respectively, obtained at 450 K. It is interesting to note that while BST alloy has its maximum S at 325 K,[18] addition of Sb$_2$O$_3$ nanoparticles shifted the maximum

S to 400 K, and further incorporation of Bi nanoprecipitates into the structure pushed the maximum S further to 450 K. This hindrance of the bipolar effect in BST/Sb$_2$O$_3$/Bi nanocomposites indicates that their good thermoelectric efficiency is stable in a wider range of temperature, as compared to pure BST. It also justifies exploring an SPB model for these nanocomposites as the minority carriers are not having a major influence on the transport properties below 450 K.

To better analyze the Seebeck coefficient data, assuming an SPB model and a relaxation time τ, the Boltzmann transport description of S was used, as shown in Equation (3):

$$S = \frac{k_B}{q}\left[\frac{\int_0^\infty \varepsilon^{\frac{3}{2}}(\varepsilon - \eta)\tau\left(\frac{\partial f}{\partial \varepsilon}\right)d\varepsilon}{\varepsilon^{\frac{3}{2}}\tau\left(\frac{\partial f}{\partial \varepsilon}\right)d\varepsilon}\right] \tag{3}$$

where ε is the reduced carrier energy ($\varepsilon = E/kT$), η is the reduced Fermi level, and τ is the carrier relaxation time associated with the net of different scattering mechanisms (as earlier mentioned in Figure S4, Supporting Information) commonly modeled by power laws, as in Equation (4):

$$\tau = \tau_0 \in^{(\lambda - 1/2)} \tag{4}$$

where λ is the scattering parameter and takes the value of 0 for acoustic phonon scattering, 1/2 for neutral impurity scattering, and 2 for ionized impurity scattering.

In the limit of the degenerate electron gas, the SPB Seebeck coefficient dependence on m* and $\overline{p}$ values can be described as Equation (5) (more details available in Figure S6, Supporting Information):

$$S = (1 + \lambda)\frac{8\pi^2 k_B^2 T}{3eh^2}m^*\left(\frac{\pi}{3\overline{p}}\right)^{2/3} \tag{5}$$

where Equation (5) was used to plot Pisarenko lines in Figure 3f. The solid lines represent charge scattering by acoustic phonons ($\lambda = 0$) for BST/Sb$_2$O$_3$/Bi nanocomposites at room temperature. However, the dashed lines represent Pisarenko lines based on the experimental S and $\overline{p}$ data, rendering slightly smaller scattering parameters. This discrepancy could be related to the contribution of polar optical phonon scattering mechanisms in addition to acoustic phonon scattering (the same logic was used to explain Figure 3d). The same trend was followed at higher temperatures (Figure S6, Supporting Information) and more negative scattering parameters were obtained. Figure 3g summarizes the calculated scattering parameters versus temperature. It is noticed that |λ| values increase by temperature in all samples, which could be another indication of the considerable involvement of polar optical phonon scattering in addition to acoustic phonon scattering mechanisms. The increased charge carrier scattering values |λ| with temperature in BST/Sb$_2$O$_3$/Bi samples can further explain the charge carrier mobility decline with temperature in Figure 3c.

To determine the electronic transport efficiency of a thermoelectric material the power factor is used, whose value

**ADVANCED
SCIENCE NEWS**

www.advancedsciencenews.com

**ADVANCED
MATERIALS
INTERFACES**

www.advmatinterfaces.de

is proportional to the Seebeck coefficient and electrical conductivity: $PF = \sigma S^2$. The temperature dependence of the power factor in BST/Sb_2O_3/Bi nanocomposites is displayed in Figure 3h. The PF in all the samples declined with temperature, due to a trade-off between the moderate increase of the Seebeck coefficient and the steep decrease of the electrical conductivity. While adding 1 wt.% Bi nanoprecipitates to BST/Sb_2O_3 did not have a considerable effect on the PF, addition of 1.5 wt.% Bi nanoprecipitates improved the PF by 20% at room temperature and this trend was observed up to 475 K. The BST/Sb_2O_3/Bi-2 sample had smaller PF compared to the BST/Sb_2O_3/Bi-1.5 sample up to 375 K due to smaller S values, but at higher temperatures, the PF of the BST/Sb_2O_3/Bi-1.5 sample was compensated by higher σ values.

The optimum electronic performance of a thermoelectric material at different temperatures depends on its weighted mobility, $\mu(m^* m_0^{-1})^{3/2}$, a factor that includes both the charge carrier mobility and density-of-states effective mass.[70] Figure 3i exhibits a comparison of the weighted mobility of the samples between 300 and 375 K. The same trend as in the PF graph (Figure 3h) was observed; with the BST/Sb_2O_3/1.5 Bi sample displaying the highest weighted mobility among the nanocomposites. This suggests that the incorporation of 1.5 wt.% additional Bi to BST/Sb_2O_3 would lead to the optimum thermoelectric performance of this nanocomposite system.

Figure 4 exhibits the thermal transport properties of BST/Sb_2O_3/Bi nanocomposites as a function of temperature. As shown in Figure 4a, the total thermal conductivity (K_{tot}) gradually declined in all samples with temperature, and after reaching a minimum value is increased. In general, a direct relationship between Bi nanoprecipitate content and K_{tot} was observed. The room temperature values of thermal conductivity in Bi-1, Bi-1.5, and Bi-2 samples were greater than that of BST/Sb_2O_3 by 7.2%, 10.9%, and 18%, respectively. Details of the thermal diffusivity and specific heat measurements used to calculate K_{tot} of the samples are provided in Figures S7 and S8, Supporting Information. The thermal diffusivity measured values were very consistent, and the maximum deviation from the average values of none of the samples was > 0.4% at all measured temperatures.

Further analysis of the thermal properties requires the decomposition of the total thermal conductivity into its major components, electronic thermal conduction (K_e) and lattice (phonon-carried) thermal conduction (K_{lat}). The electronic component of thermal conductivity was calculated from the Wiedemann–Franz law, describes as $K_e = L.\sigma.T$, in which, L is the Lorenz number described in the limit of SPB as in Equation (6):

$$L = \frac{k_B^2}{q^2} \left[\frac{(1+\lambda)(3+\lambda) F_\lambda(\eta) F_{\lambda+2}(\eta) - (2+\lambda)^2 F_{\lambda+1}^2(\eta)}{(1+\lambda)^2 F_{\lambda+1}^2(\eta)} \right] \quad (6)$$

A simpler formula to estimate the Lorenz number based on the Seebeck coefficient value has been suggested by Kim et al., described as Equation (7):[71]

$$L = 1.5 + \exp\left[\frac{-|S|}{116}\right] \quad (7)$$

using which, the discrepancy of the L values in our BST/Sb_2O_3/Bi samples compared to results from Equation (7) was <5% (Figure 4b and Figure S9, Supporting Information). It should be noted that Wiedemann–Franz law does not consider charge carrier-phonon interactions, thus is accurate at temperatures with negligible minority carrier transport. At high temperatures, the Lorenz number artificially increased due to the SPB model break down, as the thermal activation of electron-hole pairs became sizable.

Figure 4c shows that the electronic component of thermal conductivity increased significantly by adding Bi nanoprecipitates to BST/Sb_2O_3, in a similar fashion that electrical conductivity was enhanced in the samples (Figure 3a). Moreover, K_e decreased in all samples with temperature. The lattice component of thermal conductivity however showed an opposite trend, that is, the samples demonstrated a marginal increase of K_{lat} up to 375 K and then a rapid escalation at higher temperatures (Figure 4d). While most bismuth telluride-based alloys show a reduction of K_{lat} with temperature, such unusual behavior has been reported in some cases such as $Bi_{0.5}Sb_{1.5}Te_3$ alloys,[72] $Bi_{0.5}Sb_{1.5}Te_3$/Ti nanocomposites,[73] Bi_2Te_3 and Bi_2Te_3/Bi nanocomposites,[74,75] $Bi_{0.36}Sb_{1.64}Te_3$/graphene oxide nanocomposites,[76] $Bi_2(Te_{1-x}Se_x)_3$ alloys,[77] and PbTe alloys[78] without any detailed discussion. Complex theoretical calculations are required to provide further insight into this behavior, but it should also be noted that the Wiedemann–Franz law may not correctly estimate the contributions of K_e and K_{lat} in some semiconducting systems.[79] Nevertheless, one potential reason for the K_{lat} increase with temperature could be the bipolar thermal conductivity arising due to the electron-hole pairs' creation and annihilation.[80] The bipolar thermal conductivity (K_b) is defined as a function of electron- and hole-related partial conductivities and Seebeck coefficients, which tend to increase swiftly at high temperatures due to the thermal activation of minority carriers, as described by Equation (8):[81]

$$K_b = \frac{\sigma_n \sigma_p}{\sigma_n + \sigma_p} (S_p - S_n)^2 T \quad (8)$$

The Y-axis in Figure 4d is ladled $K_{lat} + K_b$ to reflect the contribution of both lattice and bipolar thermal conductivities.

The addition of Bi nanoprecipitates to BST/Sb_2O_3 decreased K_{lat}, which suggests effective phonon scattering caused by the nanoprecipitates. However, as the extra Bi had a significant influence on K_e enhancement, the total thermal conductivity increased with Bi nanoprecipitate content.

The thermoelectric figure of merit (ZT) is a measure of a material's efficiency to convert heat into electricity. It is defined as $ZT = S^2\sigma T/K_{tot}$, a net result of the competition between interdependent electronic and thermal transport phenomena. As noted in the Experimental Section, the thermal conductivity measurements on all samples were performed perpendicular to the SPS pressing axis; but, due to the small thickness of the sintered samples (disks of 10 mm diameter and 1–2 mm thickness), the rectangular bars cut for electrical conductivity and Seebeck coefficient measurements had to be analyzed parallel to the SPS pressing axis, as illustrated in **Figure 5**a,b. However, if the prepared polycrystalline samples with fine BiSbTe grains and Sb_2O_3 particles (mixed nm and µm) were assumed to have
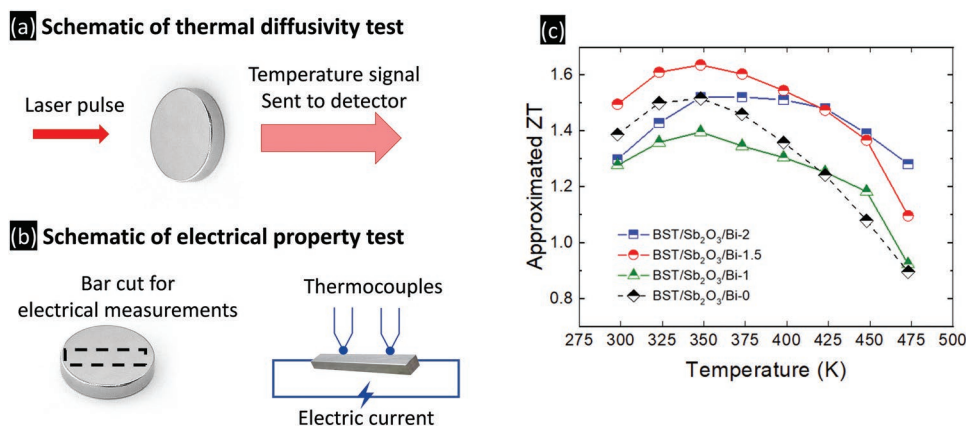
Figure 5. a,b) Schematics of thermal and electrical property measurements in relation to sample orientation. c) Approximated figure of merit versus temperature in BST/Sb$_2$O$_3$/Bi nanocomposites.

nearly isotropic properties, a plot of an approximated figure of merit versus temperature could be drawn to compare the samples' thermoelectric efficiency, regardless of the absolute ZT values. Figure 5c shows that all samples had a maximum approximated ZT at 350 K and then the ZT values decreased. This decline had a less steep rate in higher Bi nanoprecipitate content samples. The optimum near-room-temperature ZT was observed in BST/Sb$_2$O$_3$/Bi-1.5, with a max ZT at 350 K. At 425 K and above temperatures, BST/Sb$_2$O$_3$/Bi-2 demonstrated the best ZT performance. The maximum deviation from these reported ZT values was 14.9% in BST/Sb$_2$O$_3$/Bi-1, 15.6% in BST/Sb$_2$O$_3$/Bi-1.5, and 3.6% in BST/Sb$_2$O$_3$/Bi-2. While these approximated ZT values could be an overestimation, the obtained trends manifest that the BST/Sb$_2$O$_3$/Bi nanocomposites can have excellent thermoelectric efficiency for a much larger temperature range than conventional BST alloys.

3. Conclusion

In summary, p-type Bi$_{0.5}$Sb$_{1.5}$Te$_3$/Sb$_2$O$_3$ nanocomposites with additional Bi content were fabricated by an ampule sealing method, and nm and sub-nm Bi nanoprecipitates were formed in the microstructure through subsequent heat treatment. Upon mechanical grinding and ball milling, the nanocomposites powder was consolidated into disks by spark plasma sintering. The Bi nanoprecipitate content was controlled during synthesis and its effect on the thermal and electrical transport properties of Bi$_{0.5}$Sb$_{1.5}$Te$_3$/Sb$_2$O$_3$ was evaluated. The electrical conductivity and the electronic component of thermal conductivity increased by Bi nanoprecipitate content. This was attributed to additional charge carriers that were provided by Bi nanoprecipitates and were conducted via tunneling between them. The lattice thermal conductivity on the other hand declined with Bi nanoprecipitate content due to effective interfacial phonon scattering between the matrix and nanoprecipitates. The Seebeck coefficients of nanocomposites containing Bi nanoprecipitates were smaller than that of the pristine Bi$_{0.5}$Sb$_{1.5}$Te$_3$/Sb$_2$O$_3$ sample, however, the incorporation of Bi nanoprecipitates into the microstructure pushed the maximum Seebeck coefficient value from 400 to 450 K by hindering the bipolar effect. The

optimum power factor and ZT value for near room temperature (300–400 K) were obtained in Bi$_{0.5}$Sb$_{1.5}$Te$_3$/Sb$_2$O$_3$ samples with an additional 1.5 wt.% Bi nanoprecipitate content.

4. Experimental Section

Synthesis and Thermomechanical Processing of Bi$_{0.5}$Sb$_{1.5}$Te$_3$-Based Nanocomposites: Samples with a nominal composition of Bi$_{0.5}$Sb$_{1.5}$Te$_3$ (referred to as BST) were prepared from stoichiometric quantities of Bi (−100 mesh, ≥ 99.99%, Sigma Aldrich), Sb (−100 mesh, 99.5%, Sigma Aldrich), and Te (−200 mesh, > 99.8%, Sigma Aldrich) powders. Additional Bi powder equal to 1, 1.5, and 2 wt.% of the stochiometric Bi content was added to the samples labeled Bi-1, Bi-1.5, and Bi-2, respectively. The powders were mixed and sealed in an evacuated quartz ampule. An electric furnace was used to melt the ampule content at 923 K, then it was cooled to 873 K and kept at that temperature for 24 h, and finally slowly cooled to room temperature over 24 h. The solidified chunk was taken out of the ampule and mechanically milled for 1 h. The resulting powder was divided into three equal masses. The first mass was ball milled for 1 h, the second mass for 2 h, and the third mass for 4 h, separately in 50 mL grinding jars (Retsch GmbH, Germany). These milled powders, with a wide range of nm to µm sizes, were mixed with Sb$_2$O$_3$ nanoparticles (<200 nm, > 99.9%, Sigma Aldrich) at a 4 wt.% ratio. They were then loaded into a graphite die (Φ 10 mm) and sintered by spark plasma sintering (SPS-1080 System, SPS SYNTEX Inc.) under a uniaxial pressure of 46 MPa. The sintering was performed in an inert argon (Ar) atmosphere at 808 K for 5 min. Details about sintering mechanisms during the SPS process can be found in ref. [82]. The final product in each case was a disk of ≈10 mm diameter and ≈1–2 mm thickness.

Chemical and Structural Characterization: Powder XRD (Rigaku, Ultima III) with Cu Kα radiation was used to identify the compositional phases of samples. A field-emission ultra-high-resolution SEM (SU8200 Hitachi) equipped with an EDS and an energy-filtered back-scattered electron detector was used for microstructural and chemical composition analysis of the samples. A high-resolution field-emission TEM (JEOL, JEM-2100F) equipped with EDS and an annular scanning transmission electron microscope (STEM) detector was utilized for structural and localized chemical composition analyses of the samples.

Physical Property Measurements: A laser flash thermal analyzer (ULVAC TC-7000) was used to measure the thermal diffusivity coefficient (*D*) of the samples perpendicular to the SPS pressing axis. A differential scanning calorimeter (DSC, Netzsch STA 449) was used to evaluate the heat capacity (*C*$_p$). The total thermal conductivity (*k*) was then calculated using the formula $k = D.\rho.C_p$, in which ρ is the density of the samples, obtained from their mass to volume ratio. The sintered cylinders were cut into rectangular bars for simultaneous electrical conductivity and Seebeck

coefficient measurements parallel to the SPS pressing axis. A commercial instrument (ZEM-2, ULVAC Shinku-Riko) with a standard four-probe configuration under helium (He) atmosphere was used for this purpose. To ensure the physical property measurements' accuracy, three samples were tested in each compositional case, and the intermediate values were reported in the manuscript figures. The recorded values of the Seebeck coefficient, electrical conductivity, thermal diffusivity, and the specific heat capacity of other samples are provided in the electronic Supporting Information. The Hall effect measurement was carried out in a 9T physical properties measurement system (PPMS, Quantum Design), with the magnetic field sweeping from −7 to +7 T.

Supporting Information

Supporting Information is available from the Wiley Online Library or from the author.

Acknowledgements

Conflict of Interest

The authors declare no conflict of interest.

Data Availability Statement

The data that support the findings of this study are available in the supplementary material of this article.

Keywords

[1] Z. Soleimani, S. Zoras, B. Ceranic, S. Shahzad, Y. Cui, *Sustain. Energy Technol. Assess.* **2020**, *37*, 100604.
[2] T. Mori, *Small* **2017**, *13*, 1702013.
[3] T. Zhu, Y. Liu, C. Fu, J. P. Heremans, J. G. Snyder, X. Zhao, *Adv. Mater.* **2017**, *29*, 1605884.
[4] J. Mao, Z. Liu, J. Zhou, H. Zhu, Q. Zhang, G. Chen, Z. Ren, *Adv. Phys.* **2018**, *67*, 69.
[5] P. Ren, Y. Liu, J. He, T. Lv, J. Gao, G. Xu, *Inorg. Chem. Front.* **2018**, *5*, 2380.
[6] L. E. Bell, *Science* **2008**, *321*, 1457.
[7] J. He, T. M. Tritt, *Science* **2017**, *357*, aak9997.
[8] W. Liu, J. Hu, S. Zhang, M. Deng, C.-G. Han, Y. Liu, *Mater. Today Phys.* **2017**, *1*, 50.
[9] G. Prunet, F. Pawula, G. Fleury, E. Cloutet, A. J. Robinson, G. Hadziioannou, A. Pakdel, *Mater. Today Phys.* **2021**, *18*, 100402.
[10] T. Mori, S. Priya, *MRS Bull.* **2018**, *43*, 176.
[11] I. Petsagkourakis, K. Tybrandt, X. Crispin, I. Ohkubo, N. Satoh, T. Mori, *Sci. Technol. Adv. Mater.* **2018**, *19*, 836.
[12] Z. Liu, N. Sato, W. Gao, K. Yubuta, N. Kawamoto, M. Mitome, K. Kurashima, Y. Owada, K. Nagase, C.-H. Lee, J. Yi, K. Tsuchiya, T. Mori, *Joule* **2021**, *5*, 1196.
[13] S. Masoumi, S. O'Shaughnessy, A. Pakdel, *Nano Energy* **2022**, *92*, 106774.
[14] B. Cai, H. Hu, H.-L. Zhuang, J.-F. Li, *J. Alloys Compd.* **2019**, *806*, 471.
[15] B. Cai, H.-L. Zhuang, J. Pei, B. Su, J.-W. Li, H. Hu, Y. Jiang, J.-F. Li, *Nano Energy* **2021**, *85*, 106040.
[16] F. Hao, P. Qiu, Y. Tang, S. Bai, T. Xing, H.-S. Chu, Q. Zhang, P. Lu, T. Zhang, D. Ren, J. Chen, X. Shi, L. Chen, *Energy Environ. Sci.* **2016**, *9*, 3120.
[17] F. Serrano-Sánchez, M. Gharsallah, N. M. Nemes, N. Biskup, M. Varela, J. L. Martínez, M. T. Fernández-Díaz, J. A. Alonso, *Sci. Rep.* **2017**, *7*, 6277.
[18] A. Pakdel, Q. Guo, V. Nicolosi, T. Mori, *J. Mater. Chem. A* **2018**, *6*, 21341.
[19] Q. Zhang, G. Wu, Z. Guo, P. Sun, R. Wang, L. Chen, X. Wang, X. Tan, H. Hu, B. Yu, J. G. Noudem, G. Liu, J. Jiang, *ACS Appl. Mater. Interfaces* **2021**, *13*, 24937.
[20] Y. Dou, X. Yan, Y. Du, J. Xu, D. Li, *J. Mater. Sci.: Mater. Electron.* **2020**, *31*, 4808.
[21] T. Zhang, J. Jiang, Y. Xiao, Y. Zhai, S. Yang, G. Xu, *ACS Appl. Mater. Interfaces* **2013**, *5*, 3071.
[22] L. Xing, W. Cui, X. Sang, F. Hu, P. Wei, W. Zhu, X. Nie, Q. Zhang, W. Zhao, *J. Materiomics* **2021**, *7*, 998.
[23] C. Tan, X. Tan, F. Shi, Y. Yin, G.-Q. Liu, C. Xiong, H. Wang, G. Luo, B. Yu, J. G. Noudem, B. Liang, J. Jiang, *Ceram. Int.* **2021**, *47*, 725.
[24] Z. Zhang, W. Zhao, W. Zhu, S. Ma, C. Li, X. Mu, P. Wei, X. Nie, Q. Zhang, W. Zhao, *J. Electron. Mater.* **2020**, *49*, 2794.
[25] S. Y. Back, J. H. Yun, H. Cho, G. Kim, J.-S. Rhyee, *Materials* **2021**, *14*, 2506.
[26] F. Shi, H. Wang, Q. Zhang, X. Tan, Y. Yin, H. Hu, Z. Li, J. G. Noudem, G. Liu, J. Jiang, *ACS Appl. Energy Mater.* **2021**, *4*, 2944.
[27] F. Shi, C. Tan, H. Wang, X. Tan, Y. Yin, B. Yu, J. Cai, C. Xiong, G. Liu, J. Jiang, *ACS Appl. Mater. Interfaces* **2020**, *12*, 52922.
[28] Y. C. Dou, X. Y. Qin, D. Li, L. L. Li, T. H. Zou, Q. Q. Wang, *J. Appl. Phys.* **2013**, *114*, 044906.
[29] B. Madavali, H.-S. Kim, K.-H. Lee, S.-J. Hong, *Intermetallics* **2017**, *82*, 68.
[30] Y. Li, Y. Dou, X. Qin, J. Zhang, H. Xin, D. Li, C. Song, T. Zou, Y. Liu, C. Li, *RSC Adv.* **2016**, *6*, 12243.
[31] J. Li, Q. Tan, J.-F. Li, D.-W. Liu, F. Li, Z.-Y. Li, M. Zou, K. Wang, *Adv. Funct. Mater.* **2013**, *23*, 4317.
[32] L. Zhao, W. Qiu, Y. Sun, L. Chen, H. Deng, L. Yang, X. Shi, J. Tang, *J. Alloys Compd.* **2021**, *863*, 158376.
[33] B. Madavali, C. H. Lee, H. S. Kim, K. H. Lee, S. J. Hong, *Int. J. Appl. Ceram. Technol.* **2018**, *15*, 125.
[34] T. Zhang, Q. Zhang, J. Jiang, Z. Xiong, J. Chen, Y. Zhang, W. Li, G. Xu, *Appl. Phys. Lett.* **2011**, *98*, 022104.
[35] B. Madavali, D.-w. Shin, S. H. Song, D.-s. Kim, J. K. Lee, S.-J. Hong, *Mater. Chem. Phys.* **2020**, *253*, 123378.
[36] Y. Li, X. Wang, G. Liu, B. Shin, F. Shan, *Scr. Mater.* **2019**, *172*, 88.
[37] Y. Li, D. Li, X. Qin, X. Yang, Y. Liu, J. Zhang, Y. Dou, C. Song, H. Xin, *J. Mater. Chem. C* **2015**, *3*, 7045.
[38] R. Deng, X. Su, S. Hao, Z. Zheng, M. Zhang, H. Xie, W. Liu, Y. Yan, C. Wolverton, C. Uher, M. G. Kanatzidis, X. Tang, *Energy Environ. Sci.* **2018**, *11*, 1520.
[39] B. Madavali, H. S. Kim, K. H. Lee, S. J. Hong, *J. Appl. Phys.* **2017**, *121*, 225104.
[40] E. B. Kim, P. Dharmaiah, D. Shin, K.-H. Lee, S.-J. Hong, *J. Alloys Compd.* **2017**, *703*, 614.

[41] G. Yang, R. Niu, L. Sang, X. Liao, D. R. G. Mitchell, N. Ye, J. Pei, J.-F. Li, X. Wang, *Adv. Energy Mater.* **2020**, *10*, 2000757.

[42] Y. Zhang, H. Ma, B. Sun, B. Liu, H. Liu, L. Kong, B. Liu, X. Jia, X. Chen, *J. Alloys Compd.* **2017**, *715*, 344.

[43] G. Yang, L. Sang, F. F. Yun, D. R. G. Mitchell, G. Casillas, N. Ye, K. See, J. Pei, X. Wang, J.-F. Li, G. J. Snyder, X. Wang, *Adv. Funct. Mater.* **2021**, *31*, 2008851.

[44] G. Yang, L. Sang, D. R. G. Mitchell, F. Fei Yun, K. Wai See, A. Jumlat Ahmed, S. Sayyar, A. Bake, P. Liu, L. Chen, Z. Yue, D. Cortie, X. Wang, *Chem. Eng. J.* **2022**, *428*, 131205.

[45] S. Masoumi, A. Pakdel, *Adv. Eng. Mater.* **2022**, *24*, 2100955.

[46] W. Xie, X. Tang, Y. Yan, Q. Zhang, T. M. Tritt, *Appl. Phys. Lett.* **2009**, *94*, 102111.

[47] P. Dharmaiah, C. Nagarjuna, P. Sharief, S.-J. Hong, *Appl. Surf. Sci.* **2021**, *556*, 149783.

[48] F.-R. Sie, C.-S. Hwang, C.-H. Kuo, Y.-W. Chou, C.-H. Yeh, *Intermetallics* **2019**, *109*, 30.

[49] L. D. Hicks, M. S. Dresselhaus, *Phys. Rev. B* **1993**, *47*, 12727.

[50] J. J. Urban, *Nat. Nanotechnol.* **2015**, *10*, 997.

[51] C. Y. Oztan, B. Hamawandi, Y. Zhou, S. Ballikaya, M. S. Toprak, R. M. Leblanc, V. Coverstone, E. Celik, *J. Alloys Compd.* **2021**, *864*, 157916.

[52] S. T. Ahamed, C. Kulsi, Kirti, D. Banerjee, D. N. Srivastava, A. Mondal, *Surf. Interfaces* **2021**, *25*, 101149.

[53] Y. Zhao, Y. Liu, X. Sun, X. Yu, P. Zhang, X. Zhang, R. Cheng, R. Xiong, J. Shi, H. Wang, *J. Alloys Compd.* **2021**, *882*, 160697.

[54] R. Xu, L. Huang, J. Zhang, D. Li, J. Liu, J. Liu, J. Fang, M. Wang, G. Tang, *J. Mater. Chem. A* **2019**, *7*, 15757.

[55] J.-P. Issi, *Aust. J. Phys.* **1979**, *32*, 585.

[56] M. E. Toimil-Molares, T. W. Cornelius, in *Nanowires* (Ed: P. Prete), IntechOpen, London, UK **2010**.

[57] L. Li, Y. W. Yang, X. H. Huang, G. H. Li, R. Ang, L. D. Zhang, *Appl. Phys. Lett.* **2006**, *88*, 103119.

[58] J. P. Heremans, C. M. Thrush, D. T. Morelli, M.-C. Wu, *Phys. Rev. Lett.* **2002**, *88*, 216801.

[59] S. Sumithra, N. J. Takas, D. K. Misra, W. M. Nolting, P. F. P. Poudeu, K. L. Stokes, *Adv. Energy Mater.* **2011**, *1*, 1141.

[60] H. J. Goldsmid, in *2006 25th Int. Conf. on Thermoelectrics*, IEEE, Vienna, Austria **2006**.

[61] W. A. Beck, F. Crowne, J. R. Anderson, M. Gorska, Z. Dziuba, *J. Vac. Sci. Technol., A* **1988**, *6*, 2772.

[62] T.-Q. Lu, P.-F. Nan, S.-L. Song, X.-Y. Zhu, H.-Z. Zhao, Y. Deng, *Chin. Phys. B* **2018**, *27*, 047207.

[63] S. Li, T. Fan, X. Liu, F. Liu, H. Meng, Y. Liu, F. Pan, *ACS Appl. Mater. Interfaces* **2017**, *9*, 3677.

[64] A. F. May, G. J. Snyder, in *Materials, Preparation, and Characterization in Thermoelectrics* (Ed: D. M. Rowe), CRC Press, Boca Raton, FL **2017**.

[65] S. Kasap, C. Koughia, H. Ruda, R. Johanson, in *Springer Handbook of Electronic and Photonic Materials* (Eds: S. Kasap, P. Capper), Springer US, Boston, MA **2007**.

[66] Y. I. Ravich, B. A. Efimova, I. A. Smirnov, *Semiconducting Lead Chalcogenides*, Plenum Press, New York **1970**.

[67] R. Mansfield, W. Williams, *Proceedings of the Physical Society*, **1958**, *72*, 733.

[68] G. Carotenuto, C. L. Hison, F. Capezzuto, M. Palomba, P. Perlo, P. Conte, *J. Nanopart. Res.* **2008**, *11*, 1729.

[69] S. R. Hostler, Y. Q. Qu, M. T. Demko, A. R. Abramson, X. Qiu, C. Burda, *Superlattices Microstruct.* **2008**, *43*, 195.

[70] Y. Z. Pei, A. D. LaLonde, H. Wang, G. J. Snyder, *Energy Environ. Sci.* **2012**, *5*, 7963.

[71] H. S. Kim, Z. M. Gibbs, Y. L. Tang, H. Wang, G. J. Snyder, *APL Mater.* **2015**, *3*, 041506.

[72] B. Madavali, H.-S. Kim, C.-H. Lee, D.-s. Kim, S.-J. Hong, *J. Electron. Mater.* **2019**, *48*, 416.

[73] R. Deng, X. Su, Z. Zheng, W. Liu, Y. Yan, Q. Zhang, V. P. Dravid, C. Uher, M. G. Kanatzidis, X. Tang, *Sci. Adv.* **2018**, *4*, aar5606.

[74] D. K. Misra, S. Sumithra, N. S. Chauhan, W. M. Nolting, P. F. P. Poudeu, K. L. Stokes, *Mater. Sci. Semicond. Process.* **2015**, *40*, 453.

[75] W. Xie, S. Wang, S. Zhu, J. He, X. Tang, Q. Zhang, T. M. Tritt, *J. Mater. Sci.* **2013**, *48*, 2745.

[76] W. H. Shin, K. Ahn, M. Jeong, J. S. Yoon, J. M. Song, S. Lee, W. S. Seo, Y. S. Lim, *J. Alloys Compd.* **2017**, *718*, 342.

[77] S. Wang, G. Tan, W. Xie, G. Zheng, H. Li, J. Yang, X. Tang, *J. Mater. Chem.* **2012**, *22*, 20943.

[78] C. H. Su, *Mater. Today Phys.* **2018**, *5*, 58.

[79] M. Yaprintsev, R. Lyubushkin, O. Soklakova, O. Ivanov, *J. Electron. Mater.* **2018**, *47*, 1362.

[80] H. J. Goldsmid, *Proc. Phys. Soc., Sect. B* **1956**, *69*, 203.

[81] H. J. Goldsmid, *The Thermal Properties of Solids*, Dover Publications, New York **1965**.

[82] A. Pakdel, A. Witecka, G. Rydzek, D. N. Awang Shri, *Mater. Des.* **2017**, *119*, 225.